Spin polarization of edge states and the magnetosubband structure in quantum wires

S. Ihnatsenka* and I. V. Zozoulenko
Solid State Electronics, Department of Science and Technology (ITN), Linköping University, 60174 Norrköping, Sweden
(Received 3 October 2005; revised manuscript received 21 December 2005; published 28 February 2006)

We provide a quantitative description of the structure of edge states in split-gate quantum wires in the integer quantum Hall regime. We develop an effective numerical approach based on the Green's function technique for the self-consistent solution of Schrödinger equation where electron and spin interactions are included within the density functional theory in the local spin density approximation. We use the developed method to calculate the subband structure and propagating states in the quantum wires in perpendicular magnetic field starting with a geometrical layout of the wire. We discuss how the spin-resolved subband structure, the current densities, the confining potentials, as well as the spin polarization of the electron and current densities evolve when an applied magnetic field varies. We demonstrate that the exchange and correlation interactions dramatically affect the magnetosubbands in quantum wires bringing qualitatively new features in comparison to a widely used model of spinless electrons in Hartree approximation.

DOI: 10.1103/PhysRevB.73.075331 PACS number(s): 73.21.Hb, 73.43.−f, 73.23.Ad

I. INTRODUCTION

Transport properties of quantum dots, antidots, and related structures are affected by the nature of current-carrying states in the leads connecting these structures to electron reservoirs. In sufficiently high magnetic fields the current-carrying states are the edge states propagating in a close vicinity to the sample boundaries.[1] Detailed information on the structure of the edge states represents a key to the understanding of various features of the magnetotransport in the quantum Hall regime.

A quantitative description of the edge states for the case of the gate-induced confinement of the high-mobility two-dimensional electron gas (2DEG) was given by Chklovskii *et al.*,[2] who provided an analytical solution for the positions and widths of the compressible and incompressible strips arising in the 2DEG due to the electrostatic screening. In the compressible regions, the Landau bands are pinned at the Fermi energy E_F. This leads to a metallic behavior when the electron density is redistributed (compressed) to keep the electrostatic potential constant. In the incompressible regions, where the Fermi energy lies in the Landau gaps, all the levels below E_F are completely filled and hence the electron density is constant (which is consistent with the behavior of the incompressible liquid).

A number of studies addressing the problem of electron-electron interaction in quantum wires beyond the electrostatic treatment of the edge states of Chklovskii *et al.*[2] have been reported during the recent decade.[3–14] The many-body aspects of the problem have been included within Thomas-Fermi,[3] Hartree-Fock,[4–6] screened Hartree-Fock,[7] and the density functional theory.[8,9] The full quantum-mechanical calculations based on the self-consistent solution of the Schrödinger equation have been done within the Hartree[10–13] and the density functional theory[14] approximations.

Particular attention has been devoted to the investigation of the spin polarization effects in edge states.[4–8] For example, Dempsey *et al.*[5] have shown that for a sufficiently smooth confining potential, spin degeneracy of the outermost edge state is lifted and two spin channels become spatially separated. The interest in the spin-related effects in quantum wires is also motivated by significant current activity in semiconductor spintronics that utilizes the spin degree of freedom of an electron to add the additional functionality to electronic devices. A number of proposed and investigated devices for spintronics applications operates in the edge state regime,[15,16] which obviously requires a detailed knowledge of the spatial dependence of the spin-resolved states in the quantum wires. Edge states have also been proposed as one-way channels for transporting quantum information.[17] The knowledge of the spin/charge structure of the current carrying states is also essential for numerical simulation and modeling of the magnetotransport in quantum dots and related structures. (Note that such modeling is often done utilizing single-electron wave functions in the leads disregarding the spin/many-electron effects.[18–20]) In order to obtain such information on quantum-mechanical propagating states in quantum wires, one has to solve the Schrödinger equation incorporating the exchange interaction to account for the spin effects. In should be noted that the studies reported so far are often limited to some strictly integer filling factors,[5,7] or utilize Thomas-Fermi-type approaches[8] or a perturbative technique,[4,6] where the required information concerning the quantum-mechanical wave functions is not available. Moreover, the quantum-mechanical effects associated with the finite extension of the wave function (not included in, e.g., Thomas-Fermi approach) can play a decisive role for the quantitative description of the edge states. For example, Suzuki and Ando[12] have demonstrated (in a model of spinless electrons) that the predictions of Chklovskii *et al.* and Thomas-Fermi models regarding the existence and the size of the compressible/incompressible strips are in qualitative disagreement with the self-consistent modeling based on the Schrödinger equation in the regime when the estimated width of the strips is smaller than the extend of the wave functions.

The purpose of the present paper is twofold. First, we perform a detailed self-consistent solution of the Schrödinger equation incorporating spin/many-body effects in quantum

wires. We discuss how the spin-resolved subband structure, the current densities, the confining potentials, as well as the spin polarization of the electron and current densities evolve when an applied magnetic field varies. We demonstrate that the exchange and correlation interactions dramatically affect the magnetosubbands in quantum wires bringing qualitatively new features in comparison to a widely used model of spinless electrons in Hartree approximation. In the present study we limit ourselves to the regime when more than one spin-resolved state can propagate in the wire, i.e., the filling factor $\nu > 1$. (The filling factor $\nu = n/n_B = 2\pi l_B^2 n$, where n is the sheet electron density, $n_B = eB/h$ is the number of states in each Landau level per unit area, and $l_B = \sqrt{\hbar/eB}$ is the magnetic length.)

Second, we present a detailed description of the developed method based on the Green's function technique for the calculation of the subband structure and propagating states in the quantum wires in the magnetic field. This method is numerically stable, and its efficiency is related to the fact that calculations of the wave functions and wave vectors are reduced to the solution of the eigenvalue problem (as opposed to the conventional methods that require less efficient procedure of the root searching[10,11,14]). The major advantage of the present method is that it can be directly incorporated into magnetotransport calculations because it provides the eigenstates and wave vectors at the given energy, not at a given wave vector (as the conventional methods do). Besides, the present method calculates the Green's function of the wire, which can be subsequently used in the recursive Green's function technique[18,21] widely utilized for magnetotransport calculations in lateral structures.

In order to incorporate the spin/many-body effects into the Schrödinger equation we use the density functional theory (DFT) in the local spin-density approximation (LSDA).[22] The choice of the DFT is motivated, on one hand, by its efficiency and simplicity in the practical implementation within usual self-consistent formulation introduced by Kohn and Sham,[23] and, on the other hand, by its success in the reproduction of the electronic and spin properties of the low-dimensional structures in comparison to the exact diagonalization and quantum Monte Carlo calculations, as well as experiments (for a review, see Ref. 24). For example, Ferconi and Vignale[25] find that the accuracy of the DFT for the energy and density of few-electron quantum dots yields the accuracy better than 3% in comparison to the exact results. An excellent agreement between DFT and the variational Monte Carlo results for the chemical potential and the addition spectra of the rectangular quantum dot was reported by Räsänen *et al.*[26]

Within the local spin density approximation the exchange and correlation potentials are calculated using a parameterization of the functional for the exchange and correlation energy ϵ_{xc}. The latter is usually obtained on the basis of quantum Monte Carlo calculations[27,28] for the corresponding infinite homogeneous system. In the present paper we use the parameterization of Tanatar and Cerperly (TC).[27] This parameterization is valid for magnetic field when $\nu > 1$, which defines the range of applicability of our results. (Various parameterizations for ϵ_{xc} for strong fields $\nu < 1$ as well as different interpolation schemes between the low and the strong fields are reviewed in Refs. 24 and 29). Note that the DFT was used for the description of the spin polarization of the edge states in quantum wires in the integer Hall regime within the Thomas-Fermi approximation,[8] as well as for the treatment of spinless edge states in the Kohn-Sham scheme based on the solution of the Schrödinger equation.[14] The density functional theory within the Thomas-Fermi approach was also applied for the description of the edge channels in the quantum wire in the fractional Hall regime, where the parameterization of ϵ_{xc} incorporated the additional gaps that open up at the fractional filling factors.[9]

The paper is organized as follows. In Sec. II we present a formulation of the problem, where we define the geometry of the system at hand and outline the self-consistent Kohn-Sham scheme within the LSDA approximation. In Sec. III we provide a detailed description of our method based on the Green's function technique, and Sec. IV presents the major results and their discussion. The conclusions are given in Sec. V, and the Appendix presents some technical details of the calculations.

II. FORMULATION OF THE PROBLEM

We consider an infinitely long split-gate quantum wire in a perpendicular magnetic field. A schematic layout of the device is illustrated in Fig. 1(a). The distance between gates is a, the distance from the surface to the electron gas is b (we disregard the spatial extension of the electron wave function in the z direction). The donor layer with the donor density ρ_d has the width d and is situated at the distance c from the surface. The external electrostatic confinement potential can be written in the form

$$V_{conf}(y) = V_g(y) + V_d + V_{\text{Schottky}}, \tag{1}$$

where $V_g(y)$ and V_d are, respectively, potentials due to the gates[30] and the donor layer,[31] and V_{Schottky} is the Schottky barrier,

$$V_g = |V_0|\left\{1 - \frac{1}{\pi}\left[\arctan\frac{a+y}{b} + \arctan\frac{a-y}{b}\right]\right\}, \tag{2}$$

$$V_d = -\frac{e^2}{\varepsilon_0\varepsilon_r}\rho_d d(c + d/2), \tag{3}$$

with V_0 being the (negative) applied gate voltage, and ε_r being the dielectric constant. The Schottky potential and the dielectric constant are chosen to be $V_{\text{Schottky}} = 0.8$ eV and $\varepsilon_r = 13$, which is appropriate for GaAs. The external electrostatic confinement potential is shown in Fig. 1(b) for a representative quantum wire with parameters typical for an experiment. Figure 1(b) also illustrates the corresponding parabolic potential $V(y) = m^*/2(\omega y)^2$ often used to approximate the electrostatic confinement in the split-gate wires, where m^* is the effective electron mass ($m^* = 0.067 m_e$ for GaAs).

The wire is described by the effective Hamiltonian in a perpendicular magnetic field, $\mathbf{B}_\perp = B\hat{\mathbf{z}}$,

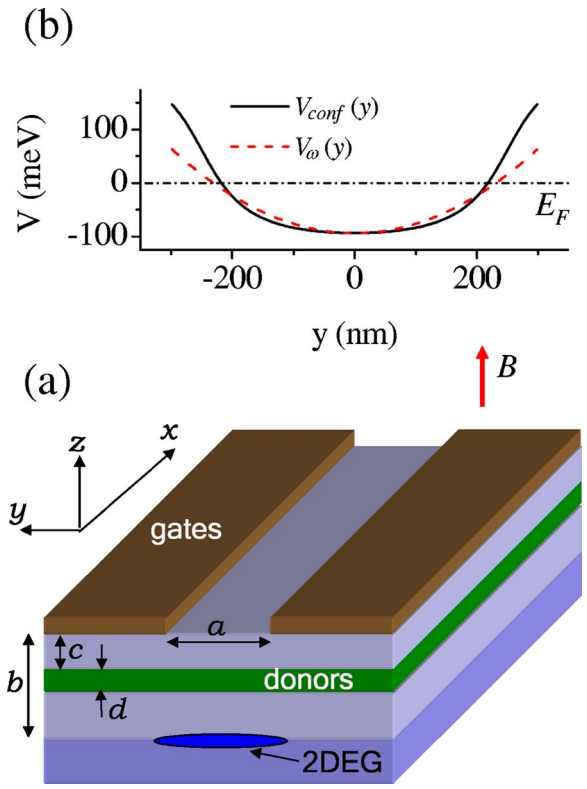

FIG. 1. (Color online) (a) A schematic layout of a split-gate quantum wire in a perpendicular magnetic field. (b) Solid line: the calculated electrostatic potential $V_{conf}(y)$ for the quantum wire with $a=500$ nm, $b=60$ nm, $c=14$ nm, $d=36$ nm, $\rho_d=6\times10^{23}$ m^{-3}, and $|V_0|=0.2$ V. A dashed line shows the corresponding parabolic confinement $V_\omega(y)=m^*(\omega y)^2/2$ (with $\hbar\omega=2$ meV) often used to approximate the external electrostatic confinement.

$$H^\sigma = H_0 + V_{conf}(y) + V^\sigma_{eff}(y) + g\mu_b B\sigma, \tag{4}$$

where H_0 is the kinetic energy in the Landau gauge, $\mathbf{A}=(-By,0,0)$,

$$H_0 = -\frac{\hbar^2}{2m^*}\left\{\left(\frac{\partial}{\partial x}-\frac{eiBy}{\hbar}\right)^2+\frac{\partial^2}{\partial^2 y}\right\}. \tag{5}$$

The last term in Eq. (4) accounts for Zeeman energy where $\mu_b=e\hbar/2m_e$ is the Bohr magneton, $\sigma=\pm\frac{1}{2}$ describes spin-up and spin-down states, $\uparrow$, $\downarrow$, and the bulk g factor of GaAs is $g=-0.44$.

The effective potential $V^\sigma_{eff}(y)$ within the framework of the Kohn-Sham density functional theory reads,[22–24]

$$V^\sigma_{eff}(\mathbf{r}) = V_H(y) + V^\sigma_{xc}(y). \tag{6}$$

$V_H(\mathbf{r})$ is the Hartree potential due to the electron density $n(y)=\Sigma_\sigma n^\sigma(y)$ (including the mirror charges),

$$V_H(y) = \frac{e^2}{4\pi\varepsilon_0\varepsilon_r}\int_{-\infty}^{+\infty}dx'\int_{-\infty}^{+\infty}dy' n(y') \times\left[\frac{1}{\sqrt{(x-x')^2+(y-y')^2}} - \frac{1}{\sqrt{(x-x')^2+(y-y')^2+4b^2}}\right] = -\frac{e^2}{4\pi\varepsilon_0\varepsilon_r}\int_{-\infty}^{+\infty}dy' n(y')\ln\frac{(y-y')^2}{(y-y')^2+4b^2}. \tag{7}$$

The exchange and correlation potential $V_{xc}(y)=V_x(y)+V_c(y)$ in the local spin density approximation is given by

$$V^\sigma_{xc} = \frac{d}{dn^\sigma}\{n^\sigma\epsilon_{xc}(n,\zeta(y))\}, \tag{8}$$

where $\zeta(y)=(n^\uparrow-n^\downarrow)/(n^\uparrow+n^\downarrow)$ is the local spin polarization. As we mentioned in the Introduction, in the present paper we use the parameterization of Tanatar and Cerperly (TC);[27] for the sake of completeness, the explicit expressions for $V_x(y)$ and $V_c(y)$ are given in the Appendix (see also Ref. 32).

III. CALCULATION OF THE ELECTRON DENSITY AND EDGE STATES IN QUANTUM WIRES

In order to calculate the self-consistent electron densities, wave functions and wave vectors of the magneto-edge states, as well as corresponding currents, we use the Green's function technique. A detailed account of the major steps of the calculations is presented in this section.

A. Hamiltonian in the mixed energy-space representation

Numerical computation of the self-consistent electron densities and other quantities of interest requires the discretization of the Hamiltonian (4). Introduce a numerical grid (lattice) with the discrete variables m,n according to $x,y \to ma,na$, where a is the lattice constant. The computational domain consists of N_s sites in the transverse n-direction (the wire is infinite in the longitudinal m-direction). Discretization of the continuous Hamiltonian (4) gives a standard tight-binding Hamiltonian with the magnetic field included in the form of the Peierls substitution,[21]

$$H^\sigma = \sum_m\left\{\sum_{n=1}^{N_s}\{\epsilon_0+V^\sigma(n)\}a^+_{m,n}a_{m,n} - t\{a^+_{m,n}a_{m,n+1}+e^{-iqn}a^+_{m,n}a_{m+1,n}+\text{H.c.}\}\right\}, \tag{9}$$

where

$$V^\sigma(n) = V_{conf}(n) + V^\sigma_{eff}(n) + g\mu_b B\sigma \tag{10}$$

is the total confining potential, the hopping element $t=\hbar^2/2m^*a^2$, the site energy $\epsilon_0=4t$, and $q=eBa^2/\hbar$; $a^+_{m,n}$ and $a_{m,n}$ denote the creation and annihilation operators at the site (m,n). The translational invariance in the longitudinal direc-

tion dictates the Bloch form for the propagating states in the quantum wire,

$$|\psi_\alpha^\sigma\rangle = \sum_m e^{ik_\alpha^\sigma m} \sum_{n=1}^{N_s} \psi_\alpha^\sigma(n) a_{m,n}^+ |0\rangle, \tag{11}$$

where the index α corresponds to the αth Bloch state with the wave vector k_α^σ and the transverse wave function $\psi_\alpha^\sigma(n)$. In Eq. (11) the wave function $\psi_\alpha^\sigma(n)$ corresponds to the real space representation. To facilitate the numerical calculation, it is convenient to expand the wave functions over the transverse eigenstates (modes) of a homogeneous wire of the width of N_s sites, $\phi_j(n) = \sqrt{2/(N_s+1)} \sin \pi jn/(N_s+1)$,

$$\psi_\alpha^\sigma(n) = \sum_{j=1}^{N} \psi_{\alpha,j}^\sigma \phi_j(n), \tag{12}$$

where the expansion coefficients $\psi_{\alpha,j}^\sigma$ can be interpreted as the wave function in the "energy" representation in the space of the transverse eigenstates.[18] Note that Eq. (12) corresponds to a conventional sin-transformation, whose inverse transform is given by the same equation.[33] The summation in Eq. (12) runs over $1 \leqslant j \leqslant N$, with $N = N_s$. In practice, however, it is sufficient to limit the summation to a much smaller number of modes, with $N \ll N_s$. Because the speed of the method is determined by the dimension of the matrices (that is given by N_s in the real space representation and N in the "energy" representation), passing to the "energy" representation greatly enhances the computational speed. For example, for the wire of the width of 0.5 μm, it is sufficient to use $N \approx 50$ modes to achieve a good convergence of the results with respect to the mode number. At the same time, in the real space representation, $N_s = 500$ (with the lattice constant $a = 1$ nm), which makes computations rather impractical.

Passing from the real space representation to the "energy" representation in the transverse direction we arrive at the Hamiltonian in the mixed energy-space representation (i.e., in the real space representation in the longitudinal m-direction and "energy" representation in the transverse n-direction),[18]

$$H = \sum_m \left\{ \sum_{j=1}^{N} \{\epsilon_j + 2t\} a_{m,j}^+ a_{m,j} + \sum_{j,j'}^{N} V_{jj'}^\sigma a_{m,j}^+ a_{m,j'} - \sum_{j,j'}^{N} [t_{jj'}^L a_{m,j}^+ a_{m+1,j'} + t_{jj'}^R a_{m+1,j}^+ a_{m,j'}] \right\}, \tag{13}$$

where $\epsilon_j = 2t - 2t \cos \pi j/N + 1$ are the eigenvalues of the transverse motion corresponding to the eigenfunctions $\phi_j(n)$; the creation and annihilation operators in the mixed space-energy representation are related to the real space creation and annihilation operators according to $a_{m,j}^+ = \Sigma_{n=1}^{N_s} \phi_j(n) a_{m,n}^+$, $a_{m,j} = \Sigma_{n=1}^{N_s} \phi_j(n) a_{m,n}$. The matrix elements of total confining potential and the hopping matrix elements are given by

$$V_{jj'}^\sigma = \sum_{n=1}^{N_s} \phi_j(n) V^\sigma(n) \phi_{j'}(n),$$

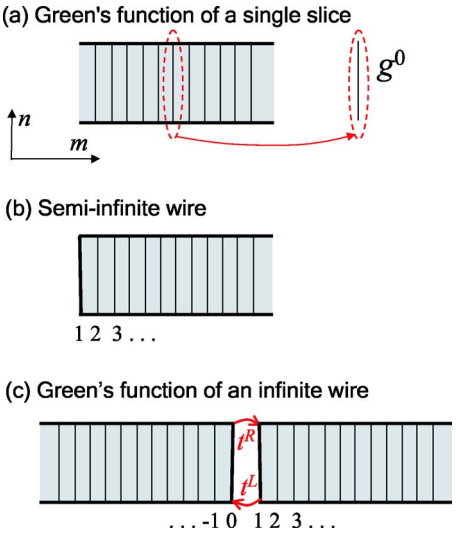

FIG. 2. (Color online) Graphical illustration of the calculations of the Green's function for a single slice (a), and for an infinite wire (b), (c).

$$t_{jj'}^R = t \sum_{n=1}^{N_s} \phi_j(n) e^{iqn} \phi_{j'}(n), \quad t_{jj'}^L = (t_{jj'}^R)^*. \tag{14}$$

Note that Hamiltonian (13) has nearest-neighbor couplings in the longitudinal m-direction [described by the two last terms in Eq. (13)]. In the transverse ("energy") direction, the magnetic field couples all states j on slice m to all states j' on neighboring slices $m+1$ and $m-1$. The Bloch wave functions (11) in the mixed space-energy representation read

$$|\psi_\alpha^\sigma\rangle = \sum_m e^{ik_\alpha^\sigma m} \sum_{j=1}^{N} \psi_{\alpha,j}^\sigma a_{m,j}^+ |0\rangle. \tag{15}$$

B. Bloch states of a quantum wire in magnetic field

Define a retarded Green's function of the Hamiltonian H in a standard way,[21,34]

$$(E - H + i\varepsilon) G = \mathbf{1}, \tag{16}$$

where $\mathbf{1}$ is a unitary operator. Calculate first the Green's function g^σ corresponding to a single slice [see Fig. 2(a)]. The Hamiltonian of mth single slice reads

$$h_m^\sigma = \sum_{j=1}^{N} \{\epsilon_j + 2t\} a_{m,j}^+ a_{m,j} + \sum_{j,j'}^{N} V_{jj'}^\sigma a_{m,j}^+ a_{m,j'}. \tag{17}$$

[Note that a single slice is not coupled to its neighbors, and hence two last terms in Eq. (13) are absent in Eq. (17).] Using this operator in the definition of Green's function (16), and taking the matrix elements $\langle 0|a_{m,j} \cdots a_{m,j'}^+|0\rangle$, we arrive at the $N \times N$ system of linear equations for the matrix elements of the Green's function of a single slice $g_{j''j'}^\sigma = \langle 0|a_{m,j} g^\sigma a_{m,j'}^+|0\rangle$,

$$\sum_{j''=1}^{N} ((E-\epsilon_j-2t)\delta_{j,j''}-V_{jj''}^{\sigma})g_{j''j'}^{\sigma}=\delta_{j,j'}. \quad (18)$$

Note that because of the translational invariance, we have dropped index m in the definition of the matrix element of the Green's function of a single slice.

Knowledge of the Green's function of a single slice g^{σ} allows one to find the Bloch states of an infinite wire. The eigenvectors $\{\psi_{j\alpha}^{\sigma}\}$ and eigenvalues $\{k_{\alpha}^{\sigma}\}$ are determined by the eigenequation[18]

$$\begin{pmatrix} -(g^{\sigma}t^{L})^{-1} & -(t^{L})^{-1}t^{R} \\ 1 & 0 \end{pmatrix}\begin{pmatrix} e^{ik}\vec{\psi}^{\sigma} \\ \vec{\psi}^{\sigma} \end{pmatrix}=e^{ik}\begin{pmatrix} e^{ik}\vec{\psi}^{\sigma} \\ \vec{\psi}^{\sigma} \end{pmatrix}, \quad (19)$$

where the matrices t^{R}, t^{L}, and g^{σ} have matrix elements given by Eqs. (14) and (18), respectively, and $\vec{\psi}^{\sigma}$ is the column vector composed of ψ_j^{σ}, $1\leqslant j\leqslant N$ [Eq. (12)]. Here and hereafter we use Greek indexes α,α' for Bloch states of the wire, and Roman indexes j,j' for the basis set of the transverse eigenfunctions $\{\phi_j(n)\}$. Equation (19) has $2N$ eigenvalues k_{α}^{σ}, $1\leqslant\alpha\leqslant N$, which can be real or complex, describing, respectively, propagating and evanescent states. (Here and hereafter k_{α}^{σ} is given in units of a^{-1} and the group velocity v is in units of a.) The eigenvalues corresponding to right propagating states $[v=\partial E/\partial k>0,\ \mathrm{Im}(k)=0]$ and states decaying to the right $[\mathrm{Im}(k)>0]$ we denote by $k_{\alpha}^{\sigma^+}$ with corresponding eigenstates $\psi_{j\alpha}^{\sigma^+}$. Correspondingly, $k_{\alpha}^{\sigma^-}$ and $\psi_{j\alpha}^{\sigma^-}$ stand for left propagating states $[v=\partial E/\partial k<0,\ \mathrm{Im}(k)=0]$ and states decaying to the left $[\mathrm{Im}(k)<0]$. Sorting right- and left-propagating eigenstates can be easily done by calculating their group velocity[18]

$$v_{\alpha}^{\sigma}=\frac{1}{\hbar}\frac{\partial E}{\partial k_{\alpha}^{\sigma}}=-\frac{2}{\hbar}\sum_{j,j'}^{N}(\psi_{j\alpha}^{\sigma})^{*}\psi_{j'\alpha}^{\sigma}\,\mathrm{Im}[e^{-ik_{\alpha}^{\sigma}}t_{jj'}^{L}]. \quad (20)$$

Passing to the real space representation for the wave functions in the above expressions and using the quantum-mechanical particle current density for αth Bloch state calculated in a standard way for a tight-binding lattice,[18]

$$j_{\alpha}^{\sigma}(n,E)=\frac{2t}{\hbar}\sin(qn+k_{\alpha}^{\sigma})|\psi_{\alpha}^{\sigma}(n)|^{2}, \quad (21)$$

the group velocity (20) can be expressed as the total particle current of αth Bloch state,

$$v_{\alpha}^{\sigma}=\sum_{n}j_{\alpha}^{\sigma}(n,E). \quad (22)$$

To conclude this section we note that a direct calculation of the eigenvectors k_{α}^{σ} and eigenfunctions $\psi_{j'\alpha}^{\sigma}$ by substitution of Eq. (15) into the Schrödinger equation and calculation of the roots of the corresponding determinant is possible (see, e.g., Refs. 10, 11, and 13). However, the procedure used here is more efficient as the solution of the eigenproblem (19) is numerically faster and less demanding than the root searching. Besides, an important advantage of the present method is that it can be directly incorporated into magnetotransport calculations, because in contrast to the root searching method, the present technique provides the eigenstates and wave vectors at the given energy, not at a given wave vector. It is also important to stress that in the magnetotransport calculations one needs a complete set of eigenfunctions including both propagating and evanescent waves. In the magnetic field the evanescent states in the quantum wires have complex k-vectors. Such solutions are not available in the conventional methods searching for the eigenstates at a given k-vector. On the other hand, the eigenequation (19) provides all the eigenvectors (both real and complex) that are subsequently sorted out as described above.

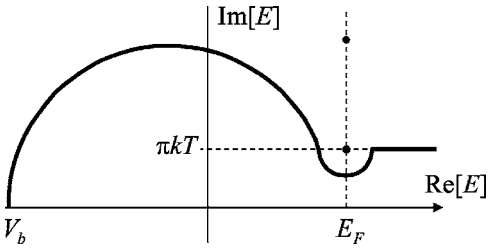

FIG. 3. A typical integration contour used in the calculation of integral (24). Dots indicate the poles of the Fermi-Dirac distribution function in the upper complex plane at $\mathrm{Re}[E]=E_F$, $\mathrm{Im}[E]=(2m+1)\pi kT$, $m=0,1,2,\ldots$.

C. Calculation of the local electron density

The diagonal elements of the total Green's function of an infinite wire in the real space representation give the local density of states (LDOS) at the site $\mathbf{r}=(m,n)$,[34]

$$\rho^{\sigma}(\mathbf{r},E)=-\frac{1}{\pi}\mathrm{Im}[G^{\sigma}(\mathbf{r},\mathbf{r},E)]. \quad (23)$$

The LDOS $\rho^{\sigma}(\mathbf{r},\mathbf{r},E)$ can be used to calculate the local electron density at the site $\mathbf{r}$,

$$n^{\sigma}(\mathbf{r})=\int_{V_b}^{\infty}dE\rho^{\sigma}(\mathbf{r},E)f(E-E_F), \quad (24)$$

where $f(E-E_F)$ is the Fermi-Dirac distribution function and the lower limit of integration V_b corresponds to the bottom of the total confining potential. Note that $\rho^{\sigma}(\mathbf{r},\mathbf{r},E)$ is a rapidly varying function of energy diverging as $\sim(E-E_{\alpha})^{-1/2}$ when E approaches the threshold subband energies E_{α}. Because of this, a direct integration along the real axis is rather ineffective as its numerical accuracy is not sufficient to achieve convergence of the self-consistent calculation of the electron density. We therefore calculate integral (24) by transforming the integration contour into the complex energy plane $\mathrm{Im}[E]>0$ where the Green's function is much more smoother than on the real axis. [Note that all poles of the Green's function (23) are in the lower half-plane $\mathrm{Im}[E]<0$.] A typical contour used in the integration avoiding poles of the Fermi-Dirac function $f(E-E_F)$ is shown in Fig. 3. We calculate the diagonal elements of the total Green's function $G^{\sigma}(\mathbf{r},\mathbf{r},E)$ as follows. We start from a semi-infinite quantum wire and calculate its surface Green's function Γ (i.e., Green's function for the boundary slice $m=1$), see Fig. 2(b).

The right and left surface Green's functions Γ^r and Γ^l (corresponding to semi-infinite wires open, respectively, to the right and left) can be written in a matrix form[18,35]

$$\Gamma^r_\sigma t^R = -\Psi^+_\sigma K^+_\sigma \Psi^{+^{-1}}_\sigma$$

$$\Gamma^l_\sigma t^L = -\Psi^-_\sigma (K^-_\sigma)^{-1} (\Psi^-_\sigma)^{-1}, \tag{25}$$

where the matrix elements $(\Psi^{+(-)}_\sigma)_{j\alpha} = \psi^{\sigma^{+(-)}}_{j\alpha}$, $(K^{+(-)}_\sigma)_{\alpha\alpha'} = \exp(k^{\sigma^{+(-)}}_\alpha)\delta_{\alpha\alpha'}$. We then connect this semi-infinite wire to the second semi-infinite wire to form an infinitely long quantum wire as shown in Fig. 2(c). The total Green's function can be calculated with the help of Dyson equation[21,34]

$$G = G^0 + G^0 U G, \tag{26}$$

where G^0 corresponds to the "unperturbed" structures (the left and right semi-infinite wires), and the operator U describes the interaction between them,

$$U = -\sum_{j,j'}^{N} [t^L_{jj'} a^+_{0,j} a_{1,j'} + t^R_{jj'} a^+_{1,j} a_{0,j'}] \tag{27}$$

[see Eq. (13)]. Using Eq. (26) to calculate the matrix element $(G^\sigma)_{jj'} = \langle 0|a_{1,j} G^\sigma a^+_{1,j'}|0\rangle$, we obtain Green's function for the slice $m=1$ (note that because of the translational invariance in the m-direction, the calculated Green's function is the same for all slices),

$$G^\sigma = (\mathbf{1} - \Gamma^r_\sigma t^R \Gamma^l_\sigma t^L)^{-1} \Gamma^r_\sigma, \tag{28}$$

where $\mathbf{1}$ is the unit matrix. Note that Eq. (28) gives Green's functions in the "energy" representation of the space of the transverse eigenstates. To obtain the Green's function in the real space representation needed to compute the electron density $n^\sigma(\mathbf{r})$ [Eq. (24)] we perform a standard change of the basis, $G^\sigma(n,n,E) = \Sigma^N_{j,j'} \varphi_j(n) G^\sigma_{jj'} \varphi_{j'}(n)$.

D. Self-consistent calculations

1. Iteration procedure

We calculate magneto-edge states and electron densities in a quantum wire in a self-consistent way, when on each iteration step a small part of a new potential (10) is mixed with the old one (from the previous iteration step),

$$V^\sigma_{i+1}(n) = (1-\epsilon) V^\sigma_i(n) + \epsilon V^\sigma_{i+1}(n), \tag{29}$$

ϵ being a small constant, $\sim 0.1-0.01$. Using this input potential we, for a given energy E, solve the eigenproblem (19) to find the Bloch states in the quantum wire. (Note that energy E is chosen in the complex plane as shown in Fig. 3.) We then use the obtained results to calculate the Green's function $G^\sigma(n,n,E)$ according to Eqs. (25)–(28). The integration of the Green's function (24) gives the electron densities $n^\sigma(\mathbf{r})$, which are subsequently used to compute the new total confining potential (10). It is typically needed ~ 1000 iteration steps to achieve our convergence criterium $|n^{i+1}_{1D} - n^i_{1D}|/(n^{i+1}_{1D} + n^i_{1D}) < 10^{-5}$, where n^i_{1D} is the one-dimensional electron density $n_{1D} = \int n(\mathbf{r}) dy$ on ith iteration step.

2. Adjustment of the Fermi energy

When the same fixed Fermi energy E_F is used for different magnetic fields B, the calculated self-consistent one-dimensional electron density changes as B varies. Depending on a particular realization of a quantum wire, one might need to adjust E_F for each B in order to keep the total electron density fixed, as magnetic field does not change the electron density in the system. However, in a typical experimental situation when a long quantum wire is connected to a 2DEG,[38] the Fermi energy in the reservoirs (not the electron density in the wire) is fixed. Because of this, in all calculations reported in the paper we keep E_F fixed (we set $E_F=0$).

Note that we have also performed calculations where E_F was adjusted to keep the electron density n^σ_{1D} constant. All the results obtained in this case (in particular, the density and current spin polarizations) are qualitatively and quantitatively similar to those obtained in the case when E_F is adjusted.

3. Bloch states, subband structure, and current density

Having calculated the total self-consisted confining potential, we can compute the Bloch wave functions and wave vectors by solving the eigenequation (19) for the whole range of energies of interest (note that for these calculations the energy has to be chosen on the real axis). Knowledge of the wave vectors for different states allows us to recover the subband structure, i.e., to calculate an overage position y^σ_α of the wave functions for different modes α,[36]

$$y^\sigma_\alpha = \frac{\hbar k^\sigma_\alpha a}{eB}. \tag{30}$$

We calculate the conductance of the wire $G^\sigma = I^\sigma / V$ on the basis of the linear-response Landauer formula,

$$I^\sigma = \frac{e^2}{h} V \sum_\alpha \int_{E^\sigma_{th\alpha}}^{\infty} dE \left(-\frac{\partial f(E-E_F)}{\partial E} \right), \tag{31}$$

where summation is performed over all propagating modes α for the spin σ, with $E^\sigma_{th\ \alpha}$ being the propagation threshold for αth mode. In order to visualize the current density we can rewrite Eq. (31) for the total current in the form $I^\sigma_\alpha = a\Sigma_n J^\sigma_\alpha(n)$, where the current density for the mode α reads

$$J^\sigma_\alpha(n) = \frac{e^2}{h} V \int dE \frac{j^\sigma_\alpha(n,E)}{v^\sigma_\alpha} \left(-\frac{\partial f(E-E_F)}{\partial E} \right), \tag{32}$$

with v^σ_α and $j^\sigma_\alpha(n,E)$ being, respectively, the group velocity and quantum-mechanical particle current density for the state α at the energy E [see Eqs. (22) and (21)], and V being the applied voltage.

IV. RESULTS AND DISCUSSION

A. Hartree approximation

To outline the role of exchange and correlation interactions we first study the magnetotransport in a quantum wire within the Hartree approximation [i.e., when $V^\sigma_{xc}(y)$ is not included in the effective potential (6), and the spin polariza-

tion is driven by Zeeman splitting of the energy levels]. In our calculations we use the parameters of a quantum wire indicated in Fig. 1 and the temperature $T=1$ K. With these parameters the effective width of the wire is ~400 nm, and the sheet electron density $n \approx 1.5 \times 10^{15}$ m^{-2}. Figure 4(a) shows the one-dimensional (1D) electron density n_{1D}^{σ} for the spin-up and spin-down electrons in the quantum wire. The pronounced feature of this dependence is a $1/B$-periodic, looplike pattern of the density spin polarization $P_n=(n_{1D}^{\uparrow}-n_{1D}^{\downarrow})/(n_{1D}^{\uparrow}+n_{1D}^{\downarrow})$ as illustrated in Fig. 4(b).

Figure 4(c) shows the number of spin-resolved subbands as a function of B. (As the calculations are done for the finite temperature T, for a given magnetic field, we count the subbands that lie in the energy interval $E \lesssim E_F+4kT$, where $4kT$ determines the energy window beyond which the Fermi-Dirac distribution rapidly decays to zero.) The pronounced feature of this dependence is that the number of subbands is always even, $N=2,4,6,\ldots$, such that the spin-up and spin-down subbands depopulate simultaneously. The comparison of Figs. 4(a)–4(c) demonstrates that the spin polarization is directly related to the magnetosubband structure: The polarization drops almost to zero at the magnetic fields when the subbands depopulate. In order to understand the origin of the spin polarization let us analyze the evolution of the subband structure as the applied magnetic field varies. Let us concentrate at the polarization loops in the field interval 1.3 T$\lesssim B \lesssim$2.6 T when the number of the spin-resolved subbands $N=4$ and the filling factor in the middle of the wire $2 \leqslant \nu(0) \leqslant 4$.

Figure 5(a) shows the spatially resolved difference in the electron densities $n^{\uparrow}(y)-n^{\downarrow}(y)$ as a function of B. When the subband number $N \geqslant 4$ (for $B \lesssim 2.6$ T), the electron density is mostly polarized in the inner region of the wire. We thus concentrate first on the formation of the compressible and incompressible strips in the inner region due to the upper subband. Figure 5(b) shows the filling factor $\nu^{\sigma}(y)$, current densities $J_{\alpha}^{\sigma}(n)$, and the magnetosubband structure for the magnetic field $B=1.35$ T. This field corresponds to the case when the fifth and sixth spin-resolved subbands just became depopulated, i.e., their bottoms are situated at $\gtrsim E_F+4kT$. The third and fourth subbands are separated from the fifth and sixth by the distance $\hbar\omega_c$ (with ω_c being the cyclotron frequency, $\hbar\omega_c \gg kT$), see Fig. 5(b). They are therefore situated below the Fermy energy and are fully populated. As a result, the electron density is constant, which corresponds to the formation of the incompressible strip. Because the spin-up and down subbands are fully filled, the corresponding electron densities are equal and the spin polarization of the electron density is zero.

When the magnetic field is raised the subbands are pushed up in the energy and the two highest spin-resolved subbands, following the Chklovslii *et al.* scenario,[2] become pinned at the Fermi energy. The subband bottoms flatten which signals the formation of the compressible strip in the middle of the wire, see Fig. 5(c). When the subband bottoms reach the energy $E \approx E_F-4kT$, the subbands become partially occupied. Partial subband occupation combined with their energy separation due to Zeeman interactions results in the different population for spin-up and down electrons. With increase of the magnetic field the filling factor decreases, but spin polarization increases until the subband bottoms approach $\sim E_F$, Fig. 5(d). This magnetic field corresponds to the maximal spin polarization $P_n \sim 3\%$. With further increase of the mag-

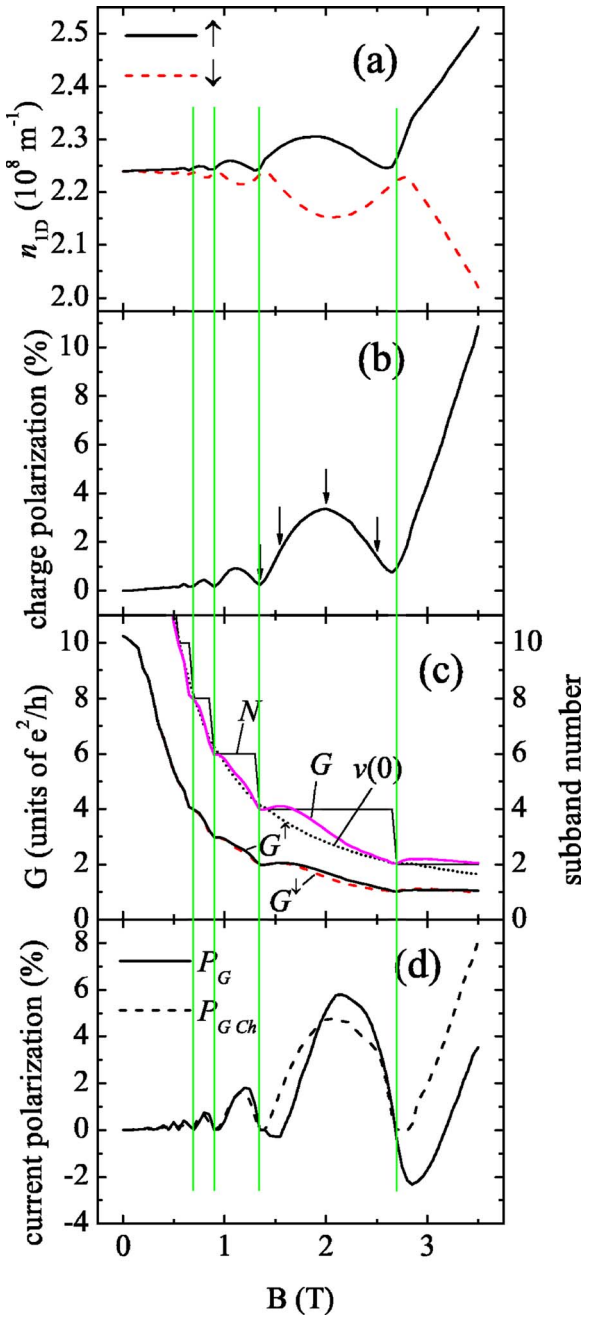

FIG. 4. (Color online) (a) One-dimensional charge density for the spin-up and spin-down electrons, $n_{1D}^{\uparrow}, n_{1D}^{\downarrow}$ in the Hartree approximation, and (b) spin polarization of the charge density, $P_n=(n_{1D}^{\uparrow}-n_{1D}^{\downarrow})/(n_{1D}^{\uparrow}+n_{1D}^{\downarrow})$, as a function of magnetic field B. (c) Total number of subbands, conductance of the spin-up and spin-down electrons, the total conductance $G=G^{\uparrow}+G^{\downarrow}$, and the filling factor in the center of the wire $\nu(0)$ [note $G_{Ch}=e^2/h\nu(0)$]. (d) The spin polarization of G and G_{Ch}. Parameters of the wire are chosen as indicated in the caption of Fig. 1. Arrows in (b) indicate the magnetic fields corresponding to the magnetosubband band structure shown in Fig. 5. Temperature $T=1$ K.

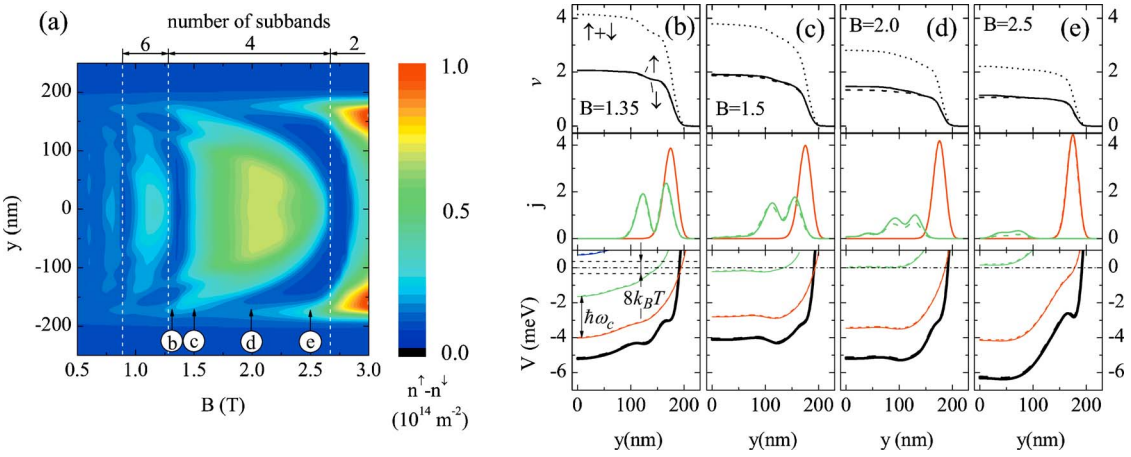

FIG. 5. (Color online) (a) Spatially resolved difference in the electron densities $n^{\uparrow}(y)-n^{\downarrow}(y)$ as a function of B calculated within Hartree approximation. (b)–(e) The subband structure for the magnetic fields indicated in (a) [see also Fig. 4(b)]. Upper panel: The filling factor $\nu(y)$ for spin-up and spin-down electrons. Middle panel: the current density distribution (in arbitrary units) for spin-up and spin-down electrons calculated according to Eq. (32). Lower panel: magnetosubband structure for spin-up and spin-down electrons (solid and dashed lines correspondingly). Fat solid and dashed lines indicate the total confining potential, Eq. (10), for, respectively, spin-up and spin-down electrons. Temperature $T=1$ K.

netic field, the subbands bottoms are pushed up above E_F, which causes further decrease of the filling factor and diminishing screening efficiency. As a result, the width of the compressible strip decreases until the upper subbands become completely depopulated and the incompressible strip forms again in the middle of the wire, see Fig. 5(e). This is accompanied by a gradual decrease of the density polarization P_n to zero. The shrinkage of the compressible strip in the middle of the wire can be also clearly traced in the evolution of the current density distribution, shown in the middle panels of Figs. 5(b)–5(e). It is interesting to note that the compressible regions are not formed for the outermost edge states corresponding to the lowest subbands $N=1$ and 2. This is because that in the field interval under study the extension of the wave function is larger than the width of the compressible strip predicted by the Chklovskii *et al.* theory.[2] The onset of the formation of the compressible strips can be seen in Fig. 5(e) for $B=2.5$ T. Note that the effect of the formation/nonformation of the compressible strips in quantum wires was discussed in detail by Suzuki and Ando for the case of spinless electrons.[12]

The described above picture of evolution of the density polarization qualitatively holds for all other polarization loops. We stress that in all the loops only two upper, partially occupied spin-resolved subbands contribute to the spin polarization, whereas remaining subbands are fully (and equally) populated and thus do no contribute to the total spin polarization. When magnetic field exceeds $B=2.6$ T, only two subbands survive in the quantum wire. With further increase of magnetic field the upper (spin-up) subband gradually depopulates and the density polarization P_n grows linearly until it reaches 100% when only the spin-down subband remains in the wire.

It should be also stressed that within Hartree approximation two outermost spin-up and spin-down edge states are not spatially polarized (i.e., they are situated at practically the same distance from the wire edges, see Fig. 5).

Figures 4(c) and 4(d) show the conductance G^{σ} for spin-up and spin-down states and its relative spin polarization $P_G=(G^{\uparrow}-G^{\downarrow})/(G^{\uparrow}+G^{\downarrow})$. The spin polarization P_G follows a similar behavior as the density polarization P_n with one subtle difference. Namely, the density polarization P_n is always positive because spin-up states always lie in energy below the corresponding spin-down states, and, therefore $n^{\uparrow}(y)-n^{\downarrow}(y)>0$. In contrast, the spin polarization of the current, after reaching zero, does not immediately rise as the magnetic field increases, but, instead, becomes negative before raising again. Note that this is accompanied by a small (but noticeable) increase of the total current [at $B\sim 1.5$ T, 3 T see Fig. 4(c)]. This effect can be traced back to the self-consistent band structure as explained below. Figure 6 shows a closeup of the upper subbands $N=3,4$ for the magnetic field $B=1.5$ T, i.e., when the current polarization is negative. Because the spin-up/down subbands are not flat, for certain energies $E<E_F$ the upper (spin-down) subband can give rise to several propagating states, whereas the lower (spin-up) subband corresponds to only one propagating state, see Fig. 6. According to the Landauer formula (31) all propagating states contribute equally to the total current. Because of this and due to the fact that the spin-down subband is situated closer to the Fermi energy, the total current for the spin-down electrons is larger than the current for the spin-up ones. This explains the negative spin polarization of the current and the increase of the total current at the magnetic fields just above the subband depopulation. We are not aware of the discussion of this effect in the current literature. The available experimental data, see, e.g., Fig. 2 of Ref. 38 showing a nonmonotonic dependence of the conductance of a quantum wire as a function of magnetic field, are consistent with the predicted behavior of the total current. Note that this feature in the conductance also survives within the DFT approach (see below, Fig. 7).

Figures 4(c) and 4(d) also show the conductance and its spin polarization calculated according to the Chklovskii *et al.*

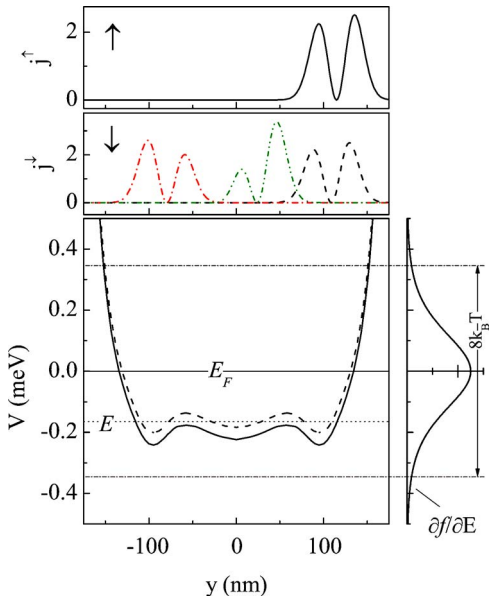

FIG. 6. (Color online) Lower panel: A closeup of the spin-up and spin-down subbands $N=3,4$ (solid and dashed lines, respectively) for the magnetic field $B=1.5$ T, when the polarization of the conductance P_G is negative. Upper panels: current density distribution (in arbitrary units) for the spin-up and spin-down electrons at the energy E indicated in the lower panel. At this energy, there is one propagating state for spin-up electrons and three propagating states for spin-down electrons. Left inset shows the derivative of the Fermi-Dirac distribution determining the weight of the contributions from the current-carrying states to the total current density at the given energy, see Eq. (32).

prescription,[2] $G_{\mathrm{Ch}}=e^2/h\nu(0)$, with $\nu(0)$ being the filling factor in the center of the wire. G_{Ch} follows the exact conductance rather well, but does not recover the steps in the conductance related to the subband depopulation (see Ref. 3 for a related discussion). G_{Ch} does not also reproduce the increase of the current and the negative conductance polarization discussed above because these features are related to the quantum-mechanical band structure.

As we mentioned before, the Hartree approximation predicts that spin-up and spin-down subbands depopulate simultaneously and thus the conductance drops in steps of $2e^2/h$ as the magnetic field increases. This is in strong disagreement with the experimental observations that demonstrate that the subbands depopulate one by one such that the conductance decreases in steps of e^2/h. We will show in the next section that accounting for the exchange and correlation interactions leads to qualitatively new features in the subband structure and brings the theory to a close agreement with experiment.

B. Density functional theory in the local spin density approximation

Figures 7 and 8 show the electron density, conductance, and subband structure for the quantum wire calculated using DFT within LSDA, Eqs. (4)–(8). Utilization of the DFT +LSDA leads to several major quantitative and qualitative

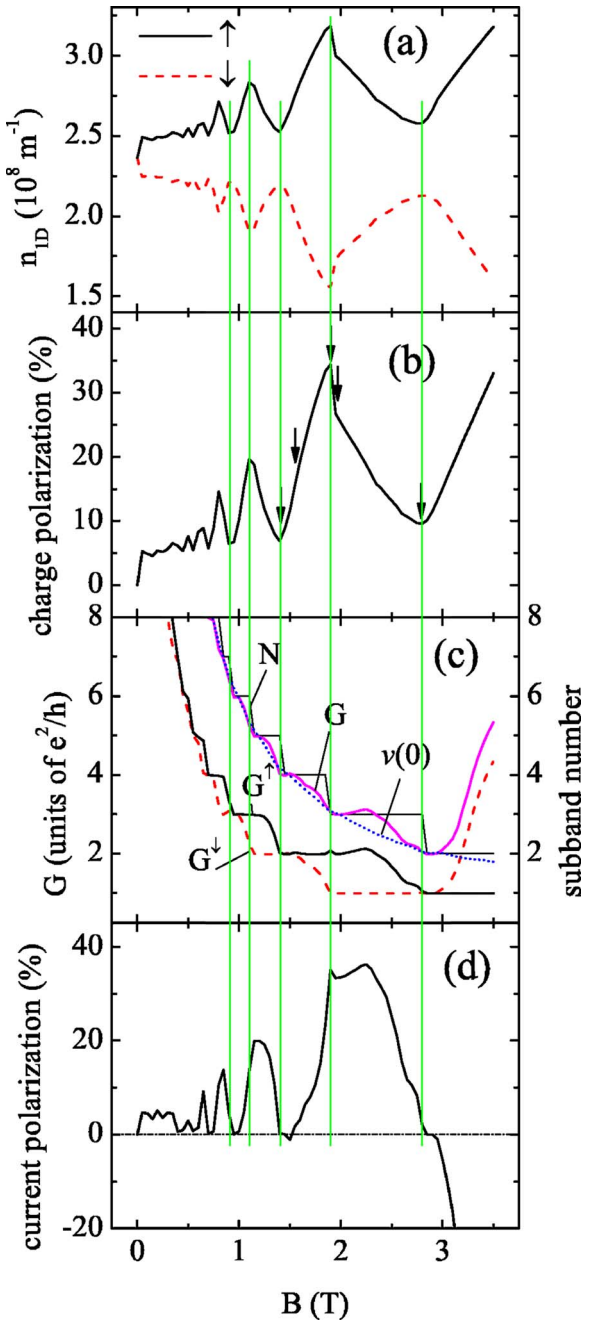

FIG. 7. (Color online). (a) One-dimensional charge density for the spin-up and spin-down electrons, $n_{1D}^{\uparrow},n_{1D}^{\downarrow}$ calculated within DFT+LSDA, and (b) spin polarization of the charge density, $P_n=(n_{1D}^{\uparrow}-n_{1D}^{\downarrow})/(n_{1D}^{\uparrow}+n_{1D}^{\downarrow})$, as a function of magnetic field B. (c) Total number of subbands, conductance of the spin-up and spin-down electrons, the total conductance $G=G^{\uparrow}+G^{\downarrow}$, and the filling factor in the center of the wire. (d) The spin polarization of the conductance P_G. Parameters of the wire are chosen as indicated in the caption to Fig. 1. Arrows in (b) indicate the magnetic fields corresponding to the magnetosubband band structure shown in Fig. 8. Temperature $T=1$ K.

differences in comparison to the Hartree approximation. First, the spin polarization of the electron density also shows a pronounced $1/B$-periodic looplike pattern. However, for the given magnetic field B the spin polarization in the quan-

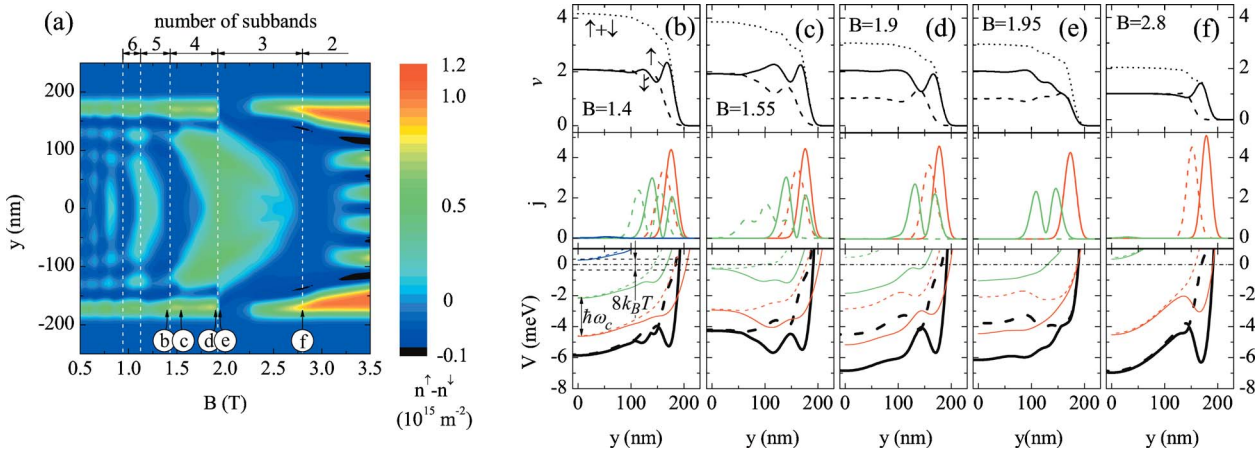

FIG. 8. (Color online) (a) Spatially resolved difference in the electron densities $n^{\uparrow}(y)-n^{\downarrow}(y)$ as a function of B calculated within DFT +LSDA. (b)–(e) The subband structure for the magnetic fields indicated in (a) [see also Fig. 7(b)]. Upper panel: The filling factor $\nu(y)$ for spin-up and spin-down electrons. Middle panel: the current density distribution (in arbitrary units) for spin-up and spin-down electrons calculated according to Eq. (32). Lower panel: magnetosubband structure for spin-up and spin-down electrons (solid and dashed lines correspondingly). Fat solid and dashed lines indicate the total confining potential, Eq. (10), for, respectively, spin-up and spin-down electrons. Temperature $T=1$ K.

tum wire calculated on the basis of DFT is of the order of magnitude higher in comparison to the Hartree approximation. Second, the magnetosubbands depopulate one by one, and the conductance decreases in steps of e^2/h (not in steps of $2e^2/h$ as in the case of Hartree approach when the spin-up and spin-down subbands depopulate simultaneously). Third, the outermost edge states become spatially polarized (separated), which is in strong contrast with the Hartree approximation, where they are situated practically at the same distance from the wire boundary.

In order to understand the effect of the exchange and correlation interactions on the evolution of the magnetosubband structure, let us now concentrate on the same field interval as studied in the previous section, i.e., when the number of the subbands lies in the interval $3 \leqslant N \leqslant 4$ and the filling factor in the middle of the wire $2 \leqslant \nu(0) \leqslant 4$, see Fig. 7. We start from the magnetic field $B=1.4$ T, where the spin polarization of the density is minimal. Similarly to the case of Hartree approximation [Fig. 5(b)], this corresponds to the case when the fifth subbands just became depopulated as shown in Fig. 8(b). However, in contrast to the Hartree approximation, where the Zeeman interaction is not strong enough to cause any significant spin polarization, in the present case the exchange interaction leads to a non-negligible spin polarization near the boundaries of the wire ($P_n \sim 7\%$). For this magnetic field the number of subbands is even, and the spin-up and spin-down subbands are fully filled in the center of the wire. As the result, the electron densities are constant, which corresponds to a formation of the incompressible strip in the center of the wire. Because the spin-up and spin-down subbands are equally occupied, spin polarization in the center of the wire is zero [Fig. 8(a)].

When the magnetic field increases, all the subbands are pushed up in energy, and the fourth subband gets pinned at E_F near the boundary of the wire, forming the compressible strip, Fig. 8(c). With increase of magnetic field, the compressible strip extends to the center of the wire, compare Figs. 8(b) and 8(c). Note that in the Hartree case the separation between the subbands caused by the Zeeman splitting is small ($\ll kT$) and hence both the subbands are pinned at E_F [see Figs. 5(c)–5(e)]. In contrast, in the present case only one of the subbands is pinned at E_F because the subband separation is determined by the exchange interaction whose magnitude can be comparable to $\hbar\omega_c$.

Figure 8(d) shows the subband structure for the magnetic field $B=1.9$ T when the spin polarization of the electron density is maximal. In this case the fourth subband is about to be depopulated and all the remaining subbands (two spin-up and one spin-down) lie below E_F. They are therefore fully populated ($2n_{1D}^{\downarrow} \approx n_{1D}^{\uparrow}$), which corresponds to the calculated polarization $P_n \sim 33\%$.

When magnetic field is increased by only 0.05 T, the density spin polarization drops by $\sim 10\%$, and the subband structure experiences dramatic changes, see Fig. 8(e). In particular, the spatial separation between the outermost spin-up and spin-down states collapses from ~ 20 nm to zero, as shown in Fig. 9. The explanation of this remarkable effect is based on the fact that the electrostatic energy is dominant for the system at hand.[2] This is illustrated in Fig. 10 which compares the electron densities and the magnetosubband structure in a quantum wire calculated within the Hartree and DFT approximations for some representative value of the magnetic field. As expected, the total electron density is practically the same in both approximations. At the same time, the magnetosubbands and the spin-up and spin-down densities vary significantly between them. It is also interesting to note that the magnetic fields corresponding to the depopulation of even subbands $N=2,4,6\ldots$ are practically the same with and without accounting for the exchange and interaction terms, compare Figs. 4(c) and 7(c). The dramatic changes in the subband structure at $B \sim 1.95$ T can be explained as follows. At $B \sim 1.9$ T the electron density near the edge of the wire is dominated by spin-up electrons, see Fig. 7(d), the upper and middle panels. When magnetic field is

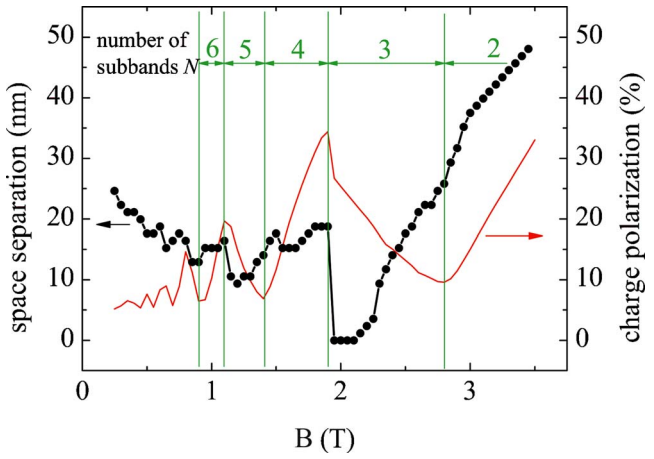

FIG. 9. (Color online) Spatial separation between the outermost spin-up and spin-down edge states as a function of magnetic field B. [The separation between the edge states is extracted from the corresponding current distribution (in arbitrary units), see Fig. 8, middle panel.] The number of subbands and the electron density spin polarization P_n from Fig. 7 is shown for comparison.

raised, the fourth subband practically depopulates, and the third (spin-up) subband is pushed up in energy. As a result, the density of the spin-up electrons associated with this subband is redistributed towards the center of the wire. However, this small change in the magnetic field cannot affect the total density. Because of this, the density of the remaining electrons has to be adjusted to keep the total density unchanged. This can be done only if the spin-down electrons associated with the subband $N=2$ are redistributed towards the edge of the wire. As a consequence of this redistribution, the densities of the spin-up (first subband) and spin-down (second subband) electrons near the wire edge become approximately equal and so does the total confining potential $V^{\sigma}(n)$, Eq. (10). The latter results in the absence of the spatial separation for the outermost edge states $N=1$ and $N=2$. Note that the effect of a collapse of the spatial separation between the outermost edge states is related to the features of the quantum-mechanical band structure, and hence is absent in the Thomas-Fermi approximation.[5,8] This effect can be utilized in spintronics devices operating in the edge state regime for injection of different spin species.[15]

The outermost spin-up and spin-down edge states remain spatially degenerate up to the magnetic field $B\sim 2.25$ T, see Figs. 8(a) and 9. The spin polarization of the electron density P_n gradually decreases in the range $1.9\ \mathrm{T}<B<2.8$ T. This decrease is related to the gradual depopulation of the third (spin-up) subband. At $B\sim 2.8$ T this subband practically depopulates, P_n reaches its minimum, and the incompressible strip is again formed in the middle of the wire [Fig. 8(f)]. With further increase of the magnetic field, the second (spin-up) subband gets pinned to E_F, and P_n gradually increases until it reaches 100% at the magnetic field when the spin-up subband depopulates.

As in the case of Hartree approximation, the evolution of the magnetosubband structure within DFT described above qualitatively holds for all other polarization loops.

Figure 7(c) shows the conductance for spin-up and spin-down electrons $G^{\uparrow}, G^{\downarrow}$, the total conductance $G=G^{\uparrow}+G^{\downarrow}$, the filling factor in the middle of the wire $\nu(0)$, and the spin polarization of the conductance. The total conductance $G(B)$ decreases in steps of e^2/h closely following the depopulation of the magnetosubbands as B increases. Note that the magnitude of $G(B)$ in plateau regions when $N>2$ shows a slight increase in comparison to the corresponding value of Ne^2/h. This effect has the same origin as in the case of Hartree approximation (see Fig. 6 and a related discussion in the text). For $N\leqslant 2$ this effect becomes much more pronounced in comparison to the Hartree approximation. This is because for magnetic fields corresponding to $N\leqslant 2$, the separation

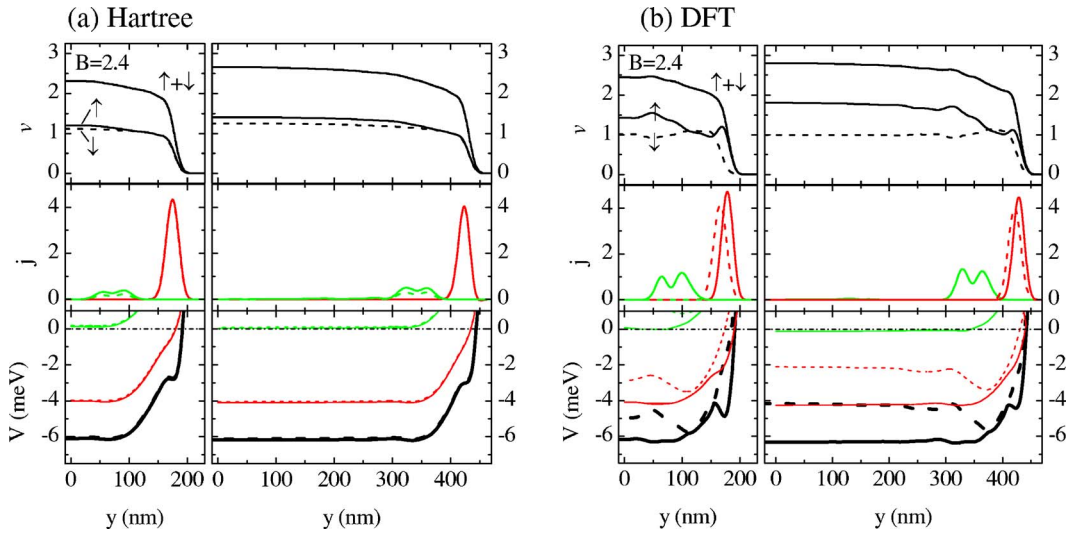

FIG. 10. (Color online) The filling factor, current densities, and the magnetosubband structure (upper, middle, and lower panels correspondingly) calculated within (a) Hartree and (b) DFT approximations for two quantum wires with different distances between the gates, $a=500$ nm (left panels), and $a=1$ μm (right panels). Remaining parameters of the wire are chosen as indicated in the caption of Fig. 1. Solid and dashed lines correspond to the spin-up and spin-down states. Fat solid and dashed lines indicate the total confining potential, Eq. (10), for, respectively, spin-up and spin-down electrons. Temperature $T=1$ K.

between bottoms of spin-up and spin-down subbands due to the exchange interaction exceeds $8kT$. Because the subbands are not flat, the spin-down subband (which is pinned to E_F) gives rise to several states propagating in the bulk of the wire as discussed in the previous section, whereas the spin-up subband (whose bottom lies well below E_F) corresponds to only one propagating state situated near the wire edge.

Note that the propagating states giving rise to the conductance for $N \leqslant 2$ are the Bloch states of an infinite quantum wire. In a typical experimental condition, a long quantum wire is connected to a much wider region of 2DEG.[38] The edge states in the region of 2DEG are coupled only to the edge states in the wire. As a result, the measured conductance for $N \leqslant 2$ does not exhibit the increase over the plateau values of Ne^2/h.[38]

Finally, we note that our analysis of the spin polarization and evolution of magnetosubbands in quantum wires was concentrated on a representative wire with the distance between the gates $a=500$ nm and the sheet electron density $n \approx 10^{15}$ m^{-2}. We would like to emphasize that all the results presented here qualitatively hold for wires of arbitrary widths and electron densities. This is illustrated in Fig. 10 for the case of two quantum wires with different distances between the gates, $a=500$ nm and $a=1$ μm, which shows practically identical subband structures as well as electron and current densities distributions.

V. CONCLUSION

In the present paper we provide a quantitative description of the structure of edge states in split-gate quantum wires in the integer quantum Hall regime. We start with a geometrical layout of the wire and calculate self-consistently quantum-mechanical magnetosubband structure and spin-resolved edge states where electron and spin interactions are included within the density functional theory in the local spin density approximation (DFT+LSDA).

We develop an effective and stable numerical method based on the Green's function technique capable of dealing with a quantum wire of arbitrary width in a high perpendicular magnetic field. The advantage of this technique is that it can be directly incorporated into magnetotransport calculations because it provides the eigenstates and wave vectors at a given energy, not at a given wave vector (as conventional methods do). Another advantage of this technique is that it calculates the Green's function of the wire, which can be subsequently used in the recursive Green's function technique widely utilized for magnetotransport calculations in lateral structures.

We use the developed method to calculate the self-consistent subband structure and propagating states in the quantum wires in a perpendicular magnetic field. We discuss how the spin-resolved subband structure, the current densities, the confining potentials, as well as the spin polarization of the electron and current densities evolve when an applied magnetic field varies. We demonstrate that the exchange and correlation interactions dramatically affect the magnetosubbands in quantum wires bringing about qualitatively new features in comparison to a widely used model of spinless electrons in Hartree approximation. These features can be summarized as follows.

(a) The spin polarization of the electron density shows a pronounced $1/B$-periodic looplike pattern, whose periodicity is related to the subband depopulation. For a given magnetic field B the spin polarization in the quantum wire calculated on the basis of DFT+LSDA is of the order of magnitude higher in comparison to the Hartree approximation (where the spin polarization is driven by the Zeeman interaction only).

(b) The magnetosubbands depopulate one by one, and the conductance decreases in steps of e^2/h (not in steps of $2e^2/h$ as in the case of Hartree approach when the spin-up and spin-down subbands depopulate practically simultaneously).

(c) The outermost spin-up and spin-down edge states become spatially polarized (separated), which is in strong contrast to the Hartree approximation, where they are situated practically at the same distance from the wire boundary. We also find that the spatial separation between the outermost edge states disappears in the range of magnetic close to filling factor $\nu=3$ and then is restored again when the magnetic field is raised. This effect can be utilized in the spintronics devices operating in the edge state regime for injection of different spin species.[15]

Recently, the structure of edge states around quantum antidots has been the subject of a lively discussion.[39] Even though the method developed in the present paper applies to quantum wires, it is reasonable to expect that for sufficiently large antidots (when the single particle level spacing Δ is smaller than kT) the present approach can also provide information on the edge state structure around the antidots.

A direct probe of spin polarization of electrons in quantum dot edge channels using polarized photoluminescence spectra has been recently reported by Nomura and Aoyagi.[40] Their method opens up a possibility for a direct probing of the electron density spin polarization in quantum wires, such that the results presented in our study [in particular the spin polarization shown in Figs. 7(b) and 8(a)], can be directly verified in the experiment.

ACKNOWLEDGMENTS

S. I. acknowledges financial support from the Royal Swedish Academy of Sciences and the Swedish Institute.

APPENDIX: EXCHANGE AND CORRELATION POTENTIALS IN THE LOCAL SPIN DENSITY APPROXIMATION

In this Appendix we provide explicit expressions for the exchange and correlation potentials entering the DFT effective potential (6). The exchange and correlation energies for 2DEG used in Eq. (8) are given by Tanatar and Ceperley (TC).[27] The exchange energy reads

$$E_{ex} = -\mathrm{Ry}^* \frac{4\sqrt{2}}{3\pi r_s}[(1+\xi)^{3/2} + (1-\xi)^{3/2}], \qquad \text{(A1)}$$

where $\zeta(y) = (n^{\uparrow} - n^{\downarrow})/n$ is the local spin-polarization, $n = n^{\uparrow} + n^{\downarrow}$ is the total electron density, and r_s is the dimensionless

TABLE I. Tabulated coefficients C_0, C_1, C_2, and C_3 (see text for detail).

	Unpolarized case (ξ=0)	Fully polarized case (ξ=1)
C_0	−0.3568	−0.0515
C_1	1.13	340.5813
C_2	0.9052	75.2293
C_3	0.4165	37.0170

density parameter which is defined in terms of the effective Bohr radius a_0^* (appropriate for a material with the effective electron mass $m^*=m_{eff}m_e$, and the dielectric constant $\varepsilon=\varepsilon_r\varepsilon_0$),

$$r_s=\frac{a}{a_0^*},\quad a=\frac{1}{\sqrt{\pi n}},\quad a_0^*=\frac{4\pi\varepsilon_r\varepsilon\hbar^2}{m_{eff}m_e e^2}=\frac{\varepsilon_r}{m_{eff}}a_0, \tag{A2}$$

where Bohr radius $a_0=0.529\times10^{-9}$ m. The factor $\mathrm{Ry}^*=m_{eff}m_e e^4/32\pi^2\varepsilon_r^2\varepsilon_0^2\hbar^2=m_{eff}/\varepsilon_r^2\mathrm{Ry}$ (1 Ry=2.17989 $\times10^{-18}$ J) generalizes TC results for the case of an arbitrary effective electron mass m^* and relative dielectric constant ε_r, and converts TC expressions[27] into SI units. The correlation energy for the unnpolarized case (ξ=0) and for the fully polarized case (ξ=1) is approximated in the form[27]

$$E_{cor}(\xi)=-\mathrm{Ry}^*C_0\frac{1+C_1w}{1+C_1w+C_2w^2+C_3w^3}, \tag{A3}$$

where $w=\sqrt{r_s}$, and the coefficients C_0, C_1, C_2, and C_3 are tabulated below (see Table I). For the case of an intermediate polarization, $0<\xi<1$, the correlation energy can be interpolated between the nonpolarized and the fully polarized cases following the receipt of von Barth and Hendin[24,37]

$$E_{cor}(\xi)=E_{cor}(0)+f(\xi)[E_{cor}(1)-E_{cor}(0)]\quad\text{with } f(\xi)=\frac{(1+\xi)^{/32}+(1-\xi)^{3/2}-2}{2^{3/2}-2}. \tag{A4}$$

Taking the functional derivatives (8) using the above expressions for the exchange and correlation energies (A1) and (A3) we arrive at the following expression for the exchange potential $V_{ex\uparrow}$, $V_{ex\downarrow}$, and for the correlation potentials used in Eq. (6),

$$V_{ex\uparrow}=-\frac{\sqrt{2}}{4}\frac{e^2}{\varepsilon_0\varepsilon_r\pi^{3/2}}\sqrt{n}\left\{[(1+\xi)^{3/2}+(1-\xi)^{3/2}]+\frac{2n^{\downarrow}}{n}[\sqrt{1+\xi}-\sqrt{1-\xi}]\right\},$$

$$V_{ex\downarrow}=-\frac{\sqrt{2}}{4}\frac{e^2}{\varepsilon_0\varepsilon_r\pi^{3/2}}\sqrt{n}\left\{[(1+\xi)^{3/2}+(1-\xi)^{3/2}]-\frac{2n^{\uparrow}}{n}[\sqrt{1+\xi}-\sqrt{1-\xi}]\right\}, \tag{A5}$$

$$V_{cor}(\xi)=V_{cor}(0)+f(\xi)[V_{cor}(1)-V_{cor}(0)],$$

$$V_{cor}(\xi=0\text{ or }\xi=1)=-\frac{m_{eff}}{\varepsilon_r^2}\mathrm{Ry}C_0\frac{1+d_1w+d_2w^2+d_3w^3+d_4w^4}{(1+C_1w+C_2w^2+C_3w^3)^2}, \tag{A6}$$

where $f(\xi)$ is given by Eq. (A4), and $d_1=2C_1$, $d_2=\left(\frac{3}{2}C_2+C_1^2\right)$, $d_3=\left(\frac{7}{4}C_3+\frac{5}{4}C_1C_2\right)$, and $d_4=\frac{3}{2}C_1C_3$.

*Permanent address: Centre of Nanoelectronics, Department of Microelectronics, Belarusian State University for Informatics and Radioelectronics., 220013 Minsk, Belarus.

[1] B. I. Halperin, Phys. Rev. B **25**, 2185 (1982).
[2] D. B. Chklovskii, B. I. Shklovskii, and L. I. Glazman, Phys. Rev. B **46**, 4026 (1992); D. B. Chklovskii, K. A. Matveev, and B. I. Shklovskii, *ibid.* **47**, 12605 (1993).
[3] K. Lier and R. R. Gerhardts, Phys. Rev. B **50**, 7757 (1994).
[4] J. M. Kinaret and P. A. Lee, Phys. Rev. B **42**, 11768 (1990).
[5] J. Dempsey, B. Y. Gelfand, and B. I. Halperin, Phys. Rev. Lett. **70**, 3639 (1993).
[6] Y. Tokura and S. Tarucha, Phys. Rev. B **50**, 10981 (1994).
[7] O. G. Balev and P. Vasilopoulos, Phys. Rev. B **56**, 6748 (1997); Z. Zhang and P. Vasilopoulos, *ibid.* **66**, 205322 (2002).
[8] T. H. Stoof and G. E. W. Bauer, Phys. Rev. B **52**, 12143 (1995).
[9] M. Ferconi, M. R. Geller, and G. Vignale, Phys. Rev. B **52**, 16357 (1995).
[10] T. Suzuki and T. Ando, J. Phys. Soc. Jpn. **62**, 2986 (1993).
[11] L. Brey, J. J. Palacios, and C. Tejedor, Phys. Rev. B **47**, 13884 (1993).
[12] T. Suzuki and T. Ando, Physica B **249-251**, 415 (1998).
[13] A. Siddiki and R. R. Gerhardts, Phys. Rev. B **70**, 195335 (2004).
[14] D. Schmerek and W. Hansen, Phys. Rev. B **60**, 4485 (1999).
[15] M. Ciorga, M. Pioro-Ladriere, P. Zawadzki, P. Hawrylak, and S. A. Sachrajda, Appl. Phys. Lett. **80**, 2177 (2002); A. S. Sachrajda, P. Hawrylak, M. Ciorga, C. Gould, and P. Zawadzki, Physica E (Amsterdam) **10**, 493 (2001).
[16] I. V. Zozoulenko and M. Evaldsson, Appl. Phys. Lett. **85**, 3136 (2004).
[17] T. M. Stace, C. H. W. Barnes, and G. J. Milburn, Phys. Rev. Lett. **93**, 126804 (2004).
[18] I. V. Zozoulenko, F. A. Maaø, and E. H. Hauge, Phys. Rev. B **53**, 7975 (1996); Phys. Rev. B **53**, 7987 (1996); Phys. Rev. B **56**, 4710 (1997).
[19] I. V. Zozoulenko, A. S. Sachrajda, C. Gould, K.-F. Berggren, P. Zawadzki, Y. Feng, and Z. Wasilewski, Phys. Rev. Lett. **83**, 1838 (1999).
[20] M. Evaldsson, I. V. Zozoulenko, M. Ciorga, P. Zawadzki, and S. A. Sachrajda, Europhys. Lett. **68**, 261 (2004).
[21] D. K. Ferry and S. M. Goodnick, *Transport in Nanostructures* (Cambridge University Press, Cambridge, England, 1997).
[22] R. G. Parr and W. Yang, *Density-Functional Theory of Atoms and*

Molecules (Oxford Science Publications, Oxford, 1989).
[23] W. Kohn and L. Sham, Phys. Rev. **140**, A1133 (1965).
[24] S. M. Reimann and M. Manninen, Rev. Mod. Phys. **74**, 1283 (2002).
[25] M. Ferconi and G. Vignale, Phys. Rev. B **50**, R14722 (1994).
[26] E. Räsänen, H. Saarikoski, V. N. Stavrou, A. Harju, M. J. Puska, and R. M. Nieminen, Phys. Rev. B **67**, 235307 (2003).
[27] B. Tanatar and D. M. Ceperley, Phys. Rev. B **39**, 5005 (1989).
[28] C. Attaccalite, S. Moroni, P. Gori-Giorgi, and G. B. Bachelet, Phys. Rev. Lett. **88**, 256601 (2002).
[29] H. Saarikoski, E. Räsänen, S. Siljamäki, A. Harju, M. J. Puska, and R. M. Nieminen, Phys. Rev. B **67**, 205327 (2003).
[30] J. Davies, I. A. Larkin, and E. V. Sukhorukov, J. Appl. Phys. **77**, 4504 (1995).
[31] J. Martorell, H. Wu, and D. W. L. Sprung, Phys. Rev. B **50**, 17298 (1994).
[32] M. Macucci, K. Hess, and G. J. Iafrate, Phys. Rev. B **48**, 17354 (1993).
[33] W. H. Press, S. A. Teukolsky, W. T. Vetterling, and B. P. Flannery, *Numerical Recipes. The Art of Scientific Computing* (Cambridge University Press, Cambridge, England, 1992).
[34] S. Datta, *Electronic Transport in Mesoscopic Systems* (Cambridge University Press, Cambridge, England, 1997).
[35] T. Ando, Phys. Rev. B **44**, 8017 (1991).
[36] J. Davies, *The Physics of Low-Dimensional Semiconductors* (Cambridge University Press, Cambridge, England, 1998).
[37] U. von Barth and L. Hedin, J. Phys. C **5**, 1629 (1972).
[38] J. Wróbel, T. Dietl, K. Regiński, and M. Bugajski, Phys. Rev. B **58**, 16252 (1998).
[39] I. Karakurt, V. J. Goldman, Jun Liu, and A. Zaslavsky, Phys. Rev. Lett. **87**, 146801 (2001); M. Kataoka and C. J. B. Ford, *ibid.* **92**, 199703 (2004); V. J. Goldman, *ibid.* **92**, 199704 (2004).
[40] S. Nomura and Y. Aoyagi, Phys. Rev. Lett. **93**, 096803 (2004).